Nanoscale

PAPER

View Article Online
View Journal | View Issue

Cite this: *Nanoscale*, 2019, **11**, 4083

All-dielectric metasurfaces for simultaneously realizing polarization rotation and wavefront shaping of visible light†

Song Gao, [a] Chul-Soon Park, [a] Sang-Shin Lee *[a] and Duk-Yong Choi [b,c]

Received 7th January 2019,
Accepted 6th February 2019

DOI: 10.1039/c9nr00187e

rsc.li/nanoscale

All-dielectric metasurfaces have shown unprecedented abilities to control light polarization and phase, yet most previous relevant studies have been mainly limited to cross-polarized schemes. This paper presents dielectric metasurfaces that incorporate distinct half-waveplate-like hydrogenated amorphous silicon nanoposts and are shown to manipulate the wavefront of transmitted visible light exhibiting controllable linear polarization angles. An anomalous beam deflector is designed, and high performances including an absolute deflection efficiency of 82%, a polarization conversion efficiency of 96%, and an extinction ratio of 37 dB are first demonstrated in the cross-polarized scheme. Furthermore, the anomalously deflected light could hold a high degree of linear polarization (>0.96), which can be continuously rotated by varying the incident polarization angle. Based on this principle, we fabricate a metalens and experimentally observe the light focusing phenomenon at the location designed for the cross-polarized light. Moreover, the rotation of the linear polarization angle corresponding to the output focused beam spot is successfully validated by tailoring the incident polarization angle. The developed metalens can therefore be treated as equivalent to the combination of a half-waveplate and focusing lens. The proposed ultra-thin dielectric metasurfaces, which do not require the alignment of multiple elements, could be used to facilitate the development of ultra-compact photonics systems.

Introduction

Metasurfaces, which are prominent planar counterparts of three-dimensional metamaterials, have garnered significant interest because of their extraordinary ability to manipulate the properties of electromagnetic waves at subwavelength scales. The fundamental elements that constitute an optical metasurface include a subwavelength-spaced nanostructure (meta-atom), which can interact with and scatter the incoming light, imparting a phase delay that is managed according to the size, shape, and orientation of the structure. Along an interface between two media, a set of meticulously designed deep-subwavelength metallic nanoantennas that were spatially allocated to induce a linearly varying phase delay (a constant phase gradient) resulted in anomalous light bending, a phenomenon that was successfully validated so that the classical Snell's law could be rewritten.[1] Thereafter, phase-gradient metasurfaces were extensively explored to manipulate the wavefront of light propagating in free space in studies relating to light focusing,[2,3] hologram generation,[4,5] and vortex beams,[6,7] among others. The idea that meta-atoms can mediate abrupt phase changes has also been applied to optical waveguides in recent years, with the intention of fulfilling diverse and intriguing functions such as optical routing and mode conversion.[8,9] In addition to the simple modulation of common light properties including the phase, amplitude and polarization,[10] metasurfaces can also be smartly devised to tailor the resonance dispersion[11] and the near-field electromagnetic wave distributions,[12,13] which can be respectively beneficial for realizing flat achromatic lenses and sensing applications.

The polarization state is critically important in many classical optics applications and has lately been recognized to play a significant role in quantum optics because quantum bits of data (qubits) can be stored in the polarization of individual photons. With the advent of metasurfaces, polarization can also serve as a vital tool for developing innovative nanophotonic devices. Recent years have witnessed the development of various bifunctional metasurfaces where two similar or distinct functionalities, such as beam steering,[14–16] light focusing,[17–19] hologram generation,[20,21] and vortex beam generation,[22,23] can be achieved when incident polarization is

[a]*Department of Electronic Engineering, Kwangwoon University, 20 Kwangwoon-ro, Nowon-gu, Seoul 01897, Republic of Korea. E-mail: slee@kw.ac.kr*
[b]*Laser Physics Centre, Research School of Physics and Engineering, Australian National University, Canberra, ACT 2601, Australia*
[c]*College of Information Science and Technology, Jinan University, Guangzhou, Guangdong, 510632, China*

† Electronic supplementary information (ESI) available: Details of the calculated effective indices and corresponding phase shifts. See DOI: 10.1039/c9nr00187e

switched from one specific state to its orthogonal counterpart. Furthermore, much recent research has been devoted to realizing metasurface-based ultra-thin polarimeters for the purpose of measuring, analyzing, and imaging light polarization.[24–29] By dividing the metasurface into several sectors, with each sector operating for a designated polarization state, different polarization components of the impinging light can be determined. In all the applications mentioned above, the polarization states of the input and output light remained the same for each functionality.

Optical waveplates are commonly used to rotate or convert light polarization in practical optical systems. With conventional waveplates made of birefringent materials, the required phase delay between the two orthogonal polarizations is attained through phase retardation accumulated over a propagation distance, which is much longer than the wavelength. Being well known for their full control over the phase and polarization, metasurfaces are undoubtedly capable of enabling significant polarization conversion with a drastically diminished thickness,[30,31] and have high potential for integrating multiple optical elements such as the waveplate, lens, and polarization beam splitter, which would advance the development of ultra-compact polarization optics. Notably, a majority of metasurfaces are reported to manipulate the wavefront of a light output whose polarization is orthogonal to that of the incident beam (cross-polarized), either by taking advantage of the geometric phase to manipulate the circularly polarized light[32] or the resonance-induced phase shift to control the linearly polarized light.[33–35] Geometric metasurfaces have been vastly explored as they hold an intrinsic ability to manipulate the wavefront of the cross-polarized light in a broadband.[32] Although the poor polarization conversion found in connection with a monolayer plasmonic metasurface can be addressed by resorting to a gap-plasmon configuration,[36,37] the operation of the metasurface remains inconveniently limited to the reflection mode. For a transmissive geometric metasurface manipulating cross-polarized light, the conversion efficiency can be remarkably elevated by taking advantage of all-dielectric materials.[2,4,38–41] However, because the metasurface's manipulation capability is solely based on the spatially variant orientations of identical meta-atoms, the resulting phase control is valid only for incident light with circular polarization,[2,4,38] and only the spatial modulation of polarization is allowed for linearly polarized incident light.[39,40] Even though the phase control of such a metasurface can be effective in a broad spectral band, the high polarization conversion efficiency can be rarely maintained over the broadband.[2] Apart from geometric metasurfaces, an ultra-thin hybrid bilayer plasmonic metasurface has also been devised to enable anomalous beam transmission with an enhanced linear polarization conversion efficiency at wavelengths near 700 nm in the visible regime.[42] The optimal conversion efficiency of the metasurface was approximately 36%, a relatively low value that may have been caused by the metal-induced dissipation loss. In most of the abovementioned studies, the desired wavefront manipulation was restricted to cross-polarized light, a severe limitation inconsistent with the original objective of integrating multiple devices. To enable both arbitrary polarization and phase control, several metasurface schemes have been proposed using paired nanoantennas,[43,44] combinations of geometric and propagation phases,[45–48] and a Fourier holography technique.[49] Another straightforward approach resorts to multiple meta-atoms with various dimensions; however, most of the relevant studies were demonstrated in the infrared regime and all were restricted to gap-plasmon metasurfaces.[33–35]

In this work, we propose and demonstrate all-dielectric metasurfaces for visible light wavefront shaping with a tailorable linear polarization state. Eight nanoposts made of hydrogenated amorphous silicon (a-Si:H) constitute the elemental meta-atoms that impart various phase delays to the incident light, playing the role of also rotating the incident light polarization angle, considering that each nanopost behaves like a half waveplate (HWP). First, the feasibility of the proposed method is verified by conceiving a beam deflector design and systematically investigating its efficiency and polarization state. We then fabricated a metasurface lens (metalens) that successfully focuses a transmitted cross-polarized beam. The linear polarization angle of the focused spot can be tuned by altering the incident polarization angle, and the monolayer metalens is considered tantamount to the combination of a conventional HWP and focusing lens (Fig. 1), which are bulky and usually need to be precisely aligned in conventional optical systems.

Results and discussion

Fig. 2a shows the configuration of the unit cell of the proposed dielectric metasurface, consisting of a rectangular a-Si:H nano-

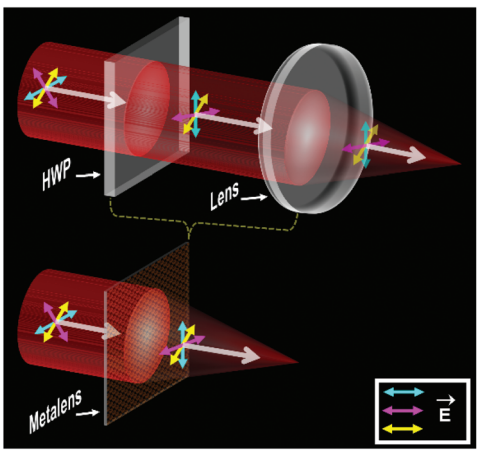

Fig. 1 Schematics of the conventional half waveplate (HWP) and lens that are usually used for polarization rotation and light focusing in optical systems (top) and a monolayer dielectric metalens that can simultaneously rotate the polarization and focus the light (bottom). The arrows in cyan, magenta and yellow color only represent the orientation of the electric field.

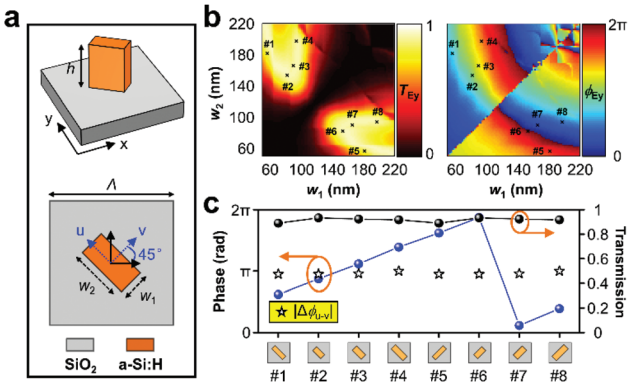

Fig. 2 (a) Schematic of an elemental unit cell of the proposed dielectric metasurface. (b) For normally *x*-polarized incident light, the calculated transmission efficiency and transmission phase for the *y*-polarized light at the designed wavelength λ = 690 nm, as a function of the nanopost dimensions (w_1 and w_2). The selected nanoposts are marked with crosses. (c) Derived transmission (black dots), phase (blue dots), and phase difference (pentagrams) between the *u*- and *v*-axes of the eight nanoposts.

post formed on an SiO_2 substrate. The adoption of a-Si:H offers the following advantages: unlike crystalline silicon, a-Si:H can be easily grown on a foreign substrate at a low temperature,[49–52] and a-Si:H exhibits a high refractive index and a low extinction coefficient ($n \approx 4.077 + 0.005i$) at the designed wavelength of 690 nm, guaranteeing efficient light manipulation at a subwavelength scale. However, when it comes to the operation at short visible wavelengths, other dielectric materials, including crystalline silicon,[53–56] titanium dioxide,[2] silicon nitride,[57] and gallium nitride,[38] are preferable to a-Si:H, which is susceptible to high absorption. Notably, except for crystalline silicon, the remaining materials have relatively lower indices which mostly restrict the meta-atoms to have near-wavelength structural heights to fulfill the entire 2π phase control. For manufacturing such devices, additional process techniques such as atomic layer deposition are usually required.[2]

Here, the unit cell's pitch was Λ = 240 nm, and the a-Si:H nanopost had a thickness of h = 320 nm, which was approximately 0.46λ. The nanopost was rotated by 45° with respect to the unit cell's *x*-axis, so that incident *x*- or *y*-polarized light could be decomposed into two orthogonal components along the *u*- and *v*-axes, representing the long and short axes of the nanopost, respectively. Supposing that a unity transmission occurred with a phase difference of $|\Delta\phi_{u-v}| = \pi$ between the *u*- and *v*-axes, incident *x*-polarized light could be completely converted to *y*-polarized light. Simulations were conducted to determine the optimal dimensions of the structures using a finite-difference time-domain method-based tool (FDTD Solutions, Lumerical, Canada). The *x*-polarized light was set to impinge normally upon the proposed unit cell, and the *y*-polarized component was examined in terms of the transmission efficiency (T_{Ey}) and phase shift (ϕ_{Ey}) by varying the dimensions (w_1, w_2) of the nanopost, as delineated in Fig. 2(b). With appropriate adjustments of the nanopost dimensions, the phase shift of the transmitted *y*-polarized light could be tuned from 0 to 2π with no significant loss, which is crucial to wavefront shaping in a cross-polarized scheme. For our demonstration, eight nanoposts (marked with crosses in Fig. 2(b)) were selected to provide a full 2π phase control. As shown in Fig. 2(c), with normally incident *x*-polarized light at the designed wavelength λ = 690 nm, the nanoposts featured nearly invariant transmission efficiencies (black dots) surpassing 89% and provided incremental phase shifts of π/4 (blue dots), both of which are related to the *y*-polarized light. For each of the selected nanoposts, the phase difference between its long and short axes was also calculated. As plotted in Fig. 2(c), the estimated phase differences (pentagrams) closely mimicked π with discrepancies within 0.05π radians, indicating that each nanopost could be treated as a near-perfect HWP at the designed wavelength, with the long (*u*-) and short (*v*-) axes of the nanopost corresponding to the slow and fast axes of the waveplate, respectively.

The dielectric nanoposts could be understood as truncated waveguides allowing the propagation of certain modes: the nanopost widths could be varied to modulate the effective index of the modes, leading to different phase shifts in the light scattered at the end of the waveguide. Because each nanopost's short and long dimensions differed, all selected nanoposts were assumed to support two effective indices (n_{eff_u} and n_{eff_v}) associated with distinct phase shifts. For each of the selected nanoposts, the effective indices of the fundamental modes were extracted from the simulations, and their corresponding phase shifts were calculated following the relationship $\phi = \frac{2\pi}{\lambda} n_{eff} h$ as illustrated in Fig. S1 of the ESI.† For each nanopost, the difference between the two effective indices led to a phase difference in the vicinity of π, which is consistent with the simulation results shown in Fig. 2(c), while for two adjacent nanoposts, the differences of their effective indices along the *u*- and *v*-axes (Δn_{eff_u} and Δn_{eff_v}) were nearly the same and both led to a near constant quarter-π phase shift.

To validate the proposed dielectric metasurface's bifunctionality in polarization conversion and wavefront shaping, an anomalous beam deflector was designed by integrating the eight nanoposts to form a supercell. A linearly increasing phase shift in intervals of π/4 was imparted across the supercell, establishing a constant phase gradient. Upon normal illumination of a plane wave polarized parallel to the *x*-axis, the *x*- and *y*-components of the electric field (E_x and E_y) were calculated, as illustrated in Fig. 3(a) and (b), respectively. The transmission profile showed that E_y was substantially stronger than E_x, indicating the conversion of the linear polarization. In addition, the field profile in Fig. 3(b) indicates a planar wavefront pertaining to an oblique propagation angle, suggesting anomalous refraction. The angle of anomalous refraction was estimated to be θ_t = 20.9°, close to the calculated angle of 21.1° as per the generalized Snell's law.[1] According to the equivalence between the generalized Snell's law and the modified diffraction equation,[58] the anomalously transmitted beam

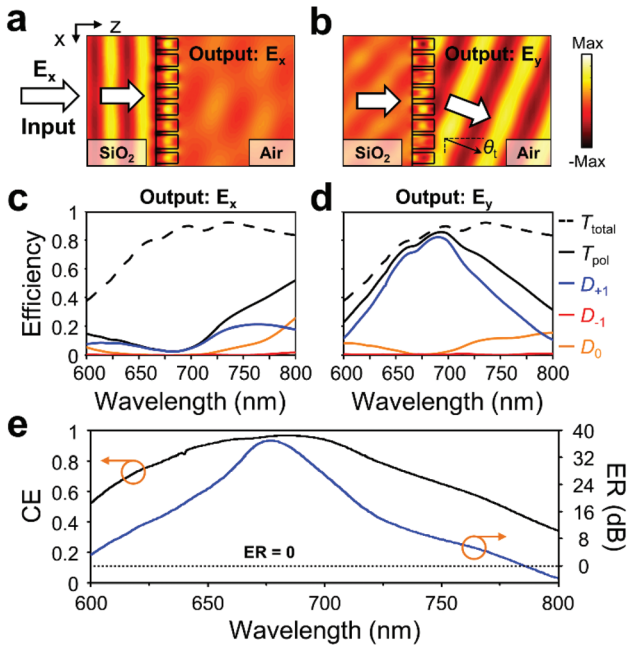

Fig. 3 Simulation results under normal incidence with polarization parallel to the *x*-axis. The simulated *xz*-plane electric field distribution relating to the (a) E_x and (b) E_y components at the wavelength of 690 nm. The polarized transmission and zeroth, positive, and negative first diffraction action spectra relating to the (c) E_x and (d) E_y components. The dashed line indicates the total transmission of the dielectric metasurface. (e) Calculated conversion efficiency (CE) and extinction ratio (ER).

matched the light wave in the first diffraction order (the positive first order in our case). Efficiencies for the polarized transmission (T_{pol}), positive first diffraction order (D_{+1}), negative first diffraction order (D_{-1}), and zeroth diffraction order (D_0) were calculated in the spectral band ranging from 600 nm to 800 nm for the E_x and E_y components, as shown in Fig. 3(c) and (d), respectively. The total transmission efficiency (T_{total}) of the proposed dielectric metasurface is shown with the dashed line in the figure for comparison. At the designed wavelength of λ = 690 nm, the total efficiency (T_{total}), E_y-polarized transmission (T_{E_ypol}) and absolute diffraction of the E_y-polarized positive first diffraction (D_{E_y+1}) were 88.6%, 85.5%, and 82.2%, respectively. The non-unity total transmission efficiency is accounted for by silicon absorption (5.4%) and the inevitable reflection (6%) from the nanoposts as these non-identical elements exhibit different reflection coefficients.[17] The performance of the beam deflector was further analyzed in terms of the conversion efficiency (CE) and extinction ratio (ER).[42] The CE is defined as the ratio of the anomalous refracted light power (D_{+1}) to the incident light power, and the ER is given as ER = 10 log(D_{E_y+1}/D_{E_x0}) in dB, where D_{E_x0} denotes the zeroth order diffraction relating to the E_x component. As plotted in Fig. 3(e), the maximum CE and ER were 96.5% and 37 dB, respectively, exceeding those of a previously reported hybrid bilayer plasmonic counterpart in a similar spectral band.[42] Although the hybrid bilayer metasurface featured an ultra-thin thickness ($\sim\lambda/6$), the thickness of our dielectric metasurface was considerably smaller *vis-à-vis* the operation wavelength ($\sim\lambda/2$). In addition, the operation bandwidth of the proposed dielectric metasurface with over 80% polarization conversion efficiency is near 100 nm, which is comparable to that of the geometric metasurface incorporating identical meta-atoms that are made of titanium dioxide nanofins.[2]

Unlike the previous dielectric metasurfaces, which are capable of manipulating cross-polarized light only with respect to a designated incident polarization,[2,4,38] the proposed metasurface could adjust the polarization of the transmitted light by altering the angle of incident polarization (Fig. 4(a)). Linearly polarized incident light can be described using the Jones vector $J_{in} = \begin{bmatrix} \cos\varphi_{in} \\ \sin\varphi_{in} \end{bmatrix}$, where φ_{in} stands for the incident polarization angle with respect to the *x*-axis. Assuming that each nanopost in the designed metasurface was an ideal HWP that could act on the incident Jones vector, the nanoposts could be represented in the form of a Jones matrix $M = \begin{bmatrix} \cos 2\alpha & \sin 2\alpha \\ \sin 2\alpha & -\cos 2\alpha \end{bmatrix}$, where α represents the angle between the fast axis of the waveplate and the *x*-axis. For the proposed dielectric metasurface with α = 45°, the linear polarization of the output transmitted light could then be expressed as

$$J_{out} = \begin{bmatrix} \cos 2\alpha & \sin 2\alpha \\ \sin 2\alpha & -\cos 2\alpha \end{bmatrix} \begin{bmatrix} \cos\varphi_{in} \\ \sin\phi_{in} \end{bmatrix} = \begin{bmatrix} \cos\left(\frac{\pi}{2} - \varphi_{in}\right) \\ \sin\left(\frac{\pi}{2} - \varphi_{in}\right) \end{bmatrix},$$

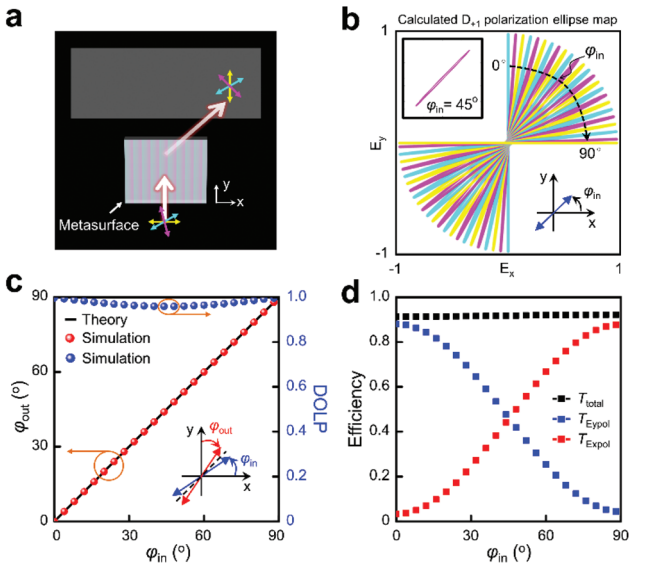

Fig. 4 (a) Illustration of a beam deflector, the output polarization state of which can be tuned by rotating the incident polarization. (b) Polarization ellipse map of the anomalously transmitted light calculated as a function of the incident polarization angle φ_{in} for the designed wavelength λ = 690 nm. The inset shows the result at φ_{in} = 45°. (c) DOLP and primary polarization angle of the output light calculated as a function of the incident polarization angle φ_{in} at a wavelength of 690 nm. (d) Total transmission and polarized transmission with the incident polarization angle φ_{in} at the wavelength 690 nm.

signifying that the input and output electric fields would have the same angle with respect to the waveplate's fast axis. For the beam deflector designed at λ = 690 nm, the polarization state pertaining to the dominant transmitted light, preserved in the first diffraction order, was analyzed based on a polarization ellipse map, with incident polarization angles being varied from φ_{in} = 0° to 90°, as shown in Fig. 4(b). For φ_{in} = 0° and 90°, the output light was linearly polarized along the *y*- and *x*-axes, respectively, whereas the output exhibited elliptical polarizations with the intermediate incident polarization angles (inset in Fig. 4(b) shows the most elliptical case at φ_{in} = 45°). The corresponding degree of linear polarization (DOLP) and primary polarization angle are calculated as shown in Fig. 4(c). The DOLP, indicative of the quality of linear polarization, is expressed as DOLP = $1 - 2\gamma/(1+\gamma^2)$, where γ represents the ratio of the lengths of the major to minor axes associated with the ellipse, and DOLP = 1 indicated a perfect linear polarization. The simulated DOLP was found to exceed 0.96, signifying a highly linear polarization. The above analysis reveals that an ideal HWP is established when the angular discrepancy between the output and input polarizations is twice the angle between the input polarization and the axis of the waveplate. Therefore, φ_{out} equals φ_{in}, as shown in the inset of Fig. 4(c). The simulated primary polarization angle matched the theoretical result. As the incident polarization was scanned from 0° to 90°, the two decomposed polarized transmissions of $T_{E_y\text{pol}}$ and $T_{E_x\text{pol}}$, respectively, decreased and increased as expected, while the total transmission remained quite stable (Fig. 4(d)). Apart from the polarization control, the transmitted beam wavefronts relating to the *x*- and *y*-polarization components were also investigated to show the wavefront control, as can be seen in Fig. S2 of the ESI.† It should be noted that for the proposed metasurface, the wavefront manipulation in the cross-polarized scheme is only valid when the incident light is *x*- or *y*-polarized. To enable constant wavefront manipulation only in the cross-polarized scheme for the incident light with an arbitrary linear polarization angle, the device is required to exhibit different fast axes corresponding to different polarization angles.

Because the HWP and focusing lens are indispensable in a variety of optical systems, we herein propose a monolayer dielectric metalens as a viable ultra-thin substitute for these two bulky components. The phase distribution for the metalens is given by $\phi(x,y) = \frac{2\pi}{\lambda}\left(f_0 - \sqrt{x^2+y^2+{f_0}^2}\right)$, where f_0 is the focal length and (x, y) represents the coordinates corresponding to the center of each unit cell affiliated with the metalens with respect to the global origin thereof $(x_0, y_0) = (0, 0)$. Fig. 5(a) shows the geometry of the designed metalens, the diameter and focal length of which were both chosen to be the same, at 60 μm each. For a normally incident *x*-polarized light, the simulated electric field intensity profiles near the focal region in both the *xz*- and *xy*-plane are shown in Fig. 5(b). The *y*-polarized light was solely focused at the expected position of *z* = 60 μm. For the designed wavelength of 690 nm, the metalens had a numerical aperture (NA) of ~0.45 and a longitudinal focal length of 4.6 μm (~6.67λ) in the *xz*-plane. In the focal plane (*xy*-plane), the focused beam spot exhibited a full-width at half-maximum (FWHM) of 720 nm, which was smaller than the diffraction limited spot size of ~770 nm (~λ/2NA).

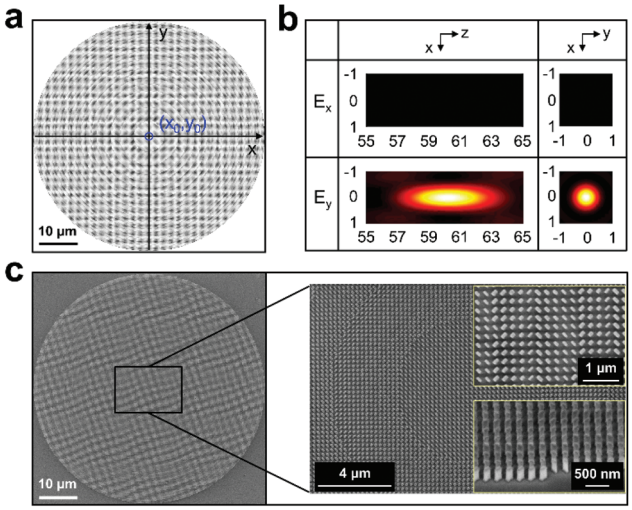

Fig. 5 (a) Geometry of the designed metalens. (b) For the designed wavelength 690 nm, the simulated electric field intensity relating to the E_x and E_y components in the *xz*-plane and *xy*-plane near and at the focal plane. (c) Scanning electron microscopy images of the metalens for illustrating the distribution of the nanoposts.

The fabrication of the designed metalens was initiated by depositing a 320 nm thick a-Si:H film on a glass substrate *via* plasma-enhanced chemical vapor deposition (Oxford, Plasmalab 100). The film was then spin-coated with an electron beam resist (ZEP520A), forming the metalens pattern with an electron beam writer (EBL, Raith150). Following electron beam evaporation of a 60 nm-thick Al layer and a subsequent lift-off process, the metalens pattern was finally transferred to the a-Si:H film *via* fluorine-based inductively coupled plasma-reactive ion etching (Oxford, Plasmalab System 100). Scanning electron microscopy images of the fabricated metalens for illustrating the distribution of the nanoposts are included in Fig. 5(c). The prepared sample was then characterized using the test setup illustrated in Fig. 6(a). A supercontinuum laser (SuperK compact, NKT Photonics) was used as an illuminator to emit broadband unpolarized light. Prior to reaching the sample, the light was converted to become linearly polarized over a narrow spectral band *via* a Glan-Thompson linear polarizer (GTH10M-A) and a narrow bandpass filter (FB690-10, with a center wavelength of 690 nm and a FWHM of 10 nm). The light transmitted from the metalens was collected *via* an objective lens that is paired with a tube lens, leading to the intensity distribution image (*xy*-plane) on a camera. An additional linear polarizer (analyzer) was incorporated so that the intensity patterns of different polarization components could be monitored.

For normally incident *x*-polarized light, a series of *y*-polarized intensity patterns were first captured by translating the imaging system along the *z*-axis in increments of 2 μm. The

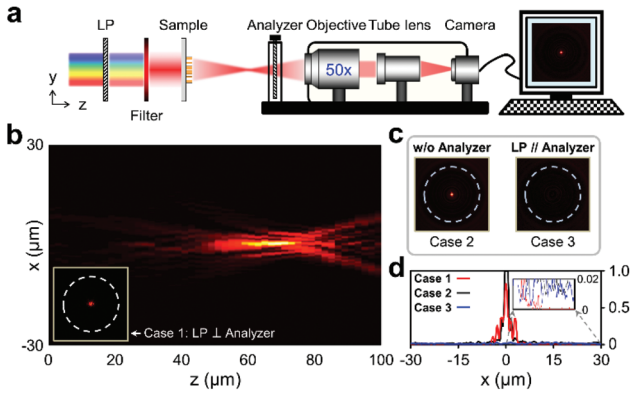

Fig. 6 (a) Measurement setup for characterizing the metalens. (b) For *x*-polarized incident light, the *y*-polarized light intensity in the *xz*-plane extracted from the measurement. The inset shows the light intensity pattern at z = 68 μm in the *xy*-plane (case 1). (c) Focus spot patterns observed in the absence of the analyzer (case 2) and when the incident polarization is parallel to the analyzer (case 3, both are *x*-polarized). (d) One-dimensional intensity distribution across the spot center from x = −30 μm to 30 μm, for all three cases. The inset shows the magnified intensity distribution from x = 0 μm to 30 μm.

metalens was placed at the position z = 0 μm, by extracting the intensity along the transverse line connecting the centers of the recorded intensity patterns, and the cross-polarized light was unequivocally revealed to be focused starting from z = 60 μm to z = 75 μm, as shown in Fig. 6(b). Because of the non-zero bandwidth of the filter and the chromatic dispersion nature of the metalens, the measured focus profile was slightly elongated compared with the simulation result shown in Fig. 5(b). The inset in the figure represents one of the cross-polarized intensity patterns (case 1) captured at z = 68 μm within the focal region, where the light passing through the metalens was focused to a bright spot at the center of the focal plane (the dashed circle in the inset corresponds to the location of the metalens) and no light is visible outside the metalens region. The non-negligible light intensity encircling the focal spot in both the figure and its inset, was supposed to be caused by the analyzer. As shown in Fig. 6(c), in the absence of the analyzer (case 2), the focused light spot featured a much finer circular shape and a uniform intensity distribution. Remarkably, the relatively weak light intensity outside of the metalens area that was invisible in case 1 is believed to originate from the incident light (*x*-polarized) because the impinging light beam was larger in size than the metalens. This can be further confirmed in case 3 when the polarization of the analyzer was set along the *x*-direction, *i.e.*, the polarization of the analyzer was parallel to the incident polarization, where a similar intensity distribution was observed except for the disappeared focus spot that was expected to be *y*-polarized. Fig. 6(d) summarizes the above analysis by plotting the one-dimensional intensity distribution across the focus center for all three cases (results for cases 1 and 2 are normalized with respect to case 3). For the focused beam spots, the peak intensity ratio between the E_y and E_x components reached a favorable level around 40. Overall, we could conclude that it was the *y*-polarized light that dominated the focused beam spot.

For the focused output light that is *y*-polarized, the intensity should be adjustable by rotating the analyzer according to Malus' law. Moreover, in contrast to the previous dielectric metalenses with fixed output polarizations,[2,41] the linear polarization of the focal spot generated by the proposed metalens could be rotated by adjusting the incident polarization angle. Here, to prove that the output polarization is rotatable, the intensity of the focused spot was monitored by rotating the linear polarizer while the polarization of the analyzer was fixed to be parallel to the *y*-axis. Fig. 7(a) shows the measured peak intensity I_{analyzer} in the focal spot when the input polarizer was rotated from φ_{in} = 0° to 180°. Both the measurement and theory indicated that the intensity vanished in the co-polarized case for φ_{in} = 90° and peaked in the cross-polarized case for φ_{in} = 0° and 180°. The phenomenon contradicted Malus' law at first glance; however, it can be understood by considering that the incident polarization angle was altered by the metalens. Moreover, the linear polarization angle of the focused output light was quantitatively examined when the input polarization was varied from φ_{in} = 0° to 90°. Given a fixed incident polarization angle, by rotating the analyzer, the output polarization could be determined when the detected intensity reached the maximum. As one may find difficulty in identifying the maximum intensity point, we chose to find the point when the intensity completely vanished, where the polarization of the analyzer was supposed to be perpendicular to that of the output polarization. Based on the above analysis, the polarization angle ($\varphi_{\text{analyzer}}$) of the analyzer, as indicated on the right-hand side of Fig. 7(b), should be equal to φ_{in}. The measured polarization angle agreed reasonably with the theoretically calculated one as shown in Fig. 7(b). The above results

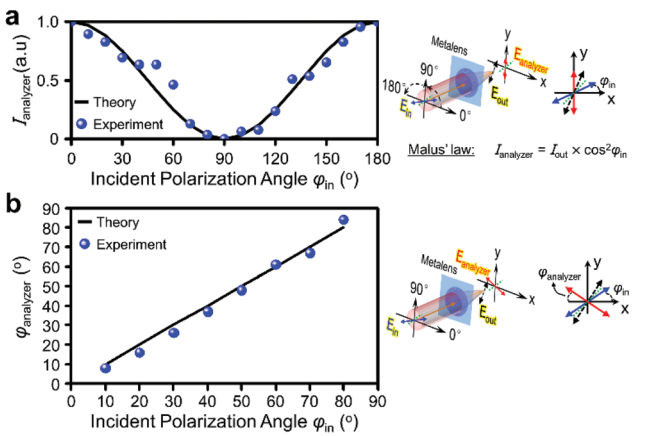

Fig. 7 (a) For the designed wavelength = 690 nm, the calculated and measured intensity in the center of the focused beam spot as a function of the incident polarization angle φ_{in} when the polarization of the analyzer is parallel to the *y*-axis. (b) For the designed wavelength = 690 nm, the calculated and measured polarization angle of the analyzer $\varphi_{\text{analyzer}}$ as a function of the incident polarization angle φ_{in}.

corroborate that the demonstrated monolayer metalens can function as both the HWP and the focusing lens. In addition to integrating multiple distinct optical devices, the simultaneous control of the light polarization and phase shift enabled by our proposed dielectric metasurface also offers strong potential for high-capacity information encryption.

Conclusions

In conclusion, all-dielectric metasurfaces were presented for concurrent realization of arbitrary linear polarization rotation and wavefront shaping in the long visible spectral band. We selected an a-Si:H material for the meta-atoms constituting the dielectric metasurface, considering its ease of fabrication, low loss, and high refractive index. Through rigorous simulations, eight nanoposts that were shown to behave like near-perfect HWPs were selected to provide full 2π phase tuning while maintaining a near-constant high transmission efficiency. We designed an anomalous beam deflector and verified its operation in the cross-polarized scheme, where it showed enhanced performances in terms of the anomalous deflection efficiency, polarization conversion efficiency, and extinction ratio. Unlike previous dielectric metasurfaces with static output polarization limited to the cross-polarization, the linear polarization of the anomalously deflected light from the proposed metasurface could be continuously rotated with a high DOLP, simply by changing the incident polarization. Based on these principles, we fabricated a metalens and experimentally observed excellent point focusing for cross-polarized transmitted light. Moreover, by tuning the input light polarization angle, the polarization of the focused spot was readily rotated. The developed metalens holds several advantages over conventional systems that combine the HWP and focusing lens, including ultra-thin thickness and no-need for alignment. The proposed metasurface could thus be considered to facilitate the development of ultimately miniaturized optical systems in the future.

Conflicts of interest

There are no conflicts to declare.

Acknowledgements

This work was supported by the National Research Foundation of Korea (NRF) grants funded by the Ministry of Science and ICT (No. 2016R1A2B2010170) and the Ministry of Education (No. 2018R1A6A1A03025242). The work was partly supported by the Australian Research Council Future Fellowship (FT110100853, Dr Duk-Yong Choi) and was performed in part at the ACT node of the Australian National Fabrication Facility. The authors are grateful to Dr Yue Sun and the National Computational Infrastructure at Australian National University for their contributions towards simulating the metalens. The authors are also grateful to Mr Woo-Bin Lee for his contributions towards preparing the experimental setup.

References

1 N. Yu, P. Genevet, M. A. Kats, F. Aieta, J. P. Tetienne, F. Capasso and Z. Gaburro, *Science*, 2011, **334**, 333–337.
2 M. Khorasaninejad, W. T. Chen, R. C. Devlin, J. Oh, A. Y. Zhu and F. Capasso, *Science*, 2016, **352**, 1190–1194.
3 X. Li, L. Chen, Y. Li, X. Zhang, M. Pu, Z. Zhao, X. Ma, Y. Wang, M. Hong and X. Luo, *Sci. Adv.*, 2016, **2**, e1601102.
4 B. Wang, F. Dong, Q. T. Li, D. Yang, C. Sun, J. Chen, Z. Song, L. Xu, W. Chu, Y. F. Xiao, Q. Gong and Y. Li, *Nano Lett.*, 2016, **16**, 5235–5240.
5 L. Huang, S. Zhang and T. Zentgraf, *Nanophotonics*, 2018, **7**, 1169–1190.
6 R. C. Devlin, A. Ambrosio, N. A. Rubin, J. P. B. Mueller and F. Capasso, *Science*, 2017, **358**, 896–901.
7 M. I. Shalaev, J. Sun, A. Tsukernik, A. Pandey, K. Nikolskiy and N. M. Litchinitser, *Nano Lett.*, 2015, **15**, 6261–6266.
8 R. Guo, M. Decker, F. Setzpfandt, X. Gai, D. Y. Choi, R. Kiselev, A. Chipouline, I. Staude, T. Pertsch, D. N. Neshev and Y. S. Kivshar, *Sci. Adv.*, 2017, **3**, e1700007.
9 Z. Li, M. H. Kim, C. Wang, Z. Han, S. Shrestha, A. C. Overvig, M. Lu, A. Stein, A. M. Agarwal, M. Loncar and N. Yu, *Nat. Nanotechnol.*, 2017, **12**, 675.
10 H. H. Hsiao, C. H. Chu and D. P. Tsai, *Small Methods*, 2017, **1**, 1600064.
11 S. Wang, P. C. Wu, V. C. Su, Y. C. Lai, M. K. Chen, H. Y. Kuo, B. H. Chen, Y. H. Chen, T. T. Huang, J. H. Wang, R. M. Lin, C. H. Kuan, T. Li, Z. Wang, S. Zhu and D. P. Tsai, *Nat. Nanotechnol.*, 2018, **13**, 227–232.
12 P. C. Wu, C. Y. Liao, V. Savinov, T. L. Chung, W. T. Chen, Y. W. Huang, P. R. Wu, Y. H. Chen, A. Q. Liu, N. I. Zheludev and D. P. Tsai, *ACS Nano*, 2018, **12**, 1920–1927.
13 W. Tang, L. Wang, X. Chen, C. Liu, A. Yu and W. Lu, *Nanoscale*, 2016, **8**, 15196.
14 F. Ding, R. Deshpande and S. I. Bozhevolnyi, *Light: Sci. Appl.*, 2018, **7**, 17178.
15 S. Liu, T. J. Cui, A. Noor, Z. Tao, H. C. Zhang, G. D. Bai, Y. Yang and X. Y. Zhou, *Light: Sci. Appl.*, 2018, **7**, 18008.
16 H. Zhang, X. Zhang, Q. Xu, C. Tian, Q. Wang, Y. Xu, Y. Li, J. Gu, Z. Tian, C. Ouyang, X. Zhang, C. Hu, J. Han and W. Zhang, *Adv. Opt. Mater.*, 2018, **6**, 1700773.
17 E. Schonbrun, K. Seo and K. B. Crozier, *Nano Lett.*, 2011, **11**, 4299–4303.
18 S. Boroviks, R. A. Deshpande, N. A. Mortensen and S. I. Bozhevolnyi, *ACS Photonics*, 2018, **5**, 1648–1653.
19 C. Williams, Y. Montelongo and T. D. Wilkinson, *Adv. Opt. Mater.*, 2017, **5**, 1700811.
20 W. T. Chen, K. Y. Yang, C. M. Wang, Y. W. Huang, S. Sun, I. D. Chiang, C. Y. Liao, W. L. Hsu, H. T. Lin, S. Sun, L. Zhou, A. Q. Liu and D. P. Tsai, *Nano Lett.*, 2013, **14**, 225–230.

21 Y. Montelongo, J. O. Tenorigo-Pearl, W. I. Milne and T. D. Wilkinson, *Nano Lett.*, 2013, **14**, 294–298.
22 A. Arbabi, Y. Horie, M. Bagheri and A. Faraon, *Nat. Nanotechnol.*, 2015, **10**, 937–943.
23 F. Zhang, H. Yu, J. Fang, M. Zhang, S. Chen, J. Wang, A. He and J. Chen, *Opt. Express*, 2016, **24**, 6656–6664.
24 A. Pors, M. G. Nielsen and S. I. Bozhevolnyi, *Optica*, 2015, **2**, 716–723.
25 F. Ding, A. Pors, Y. Chen, V. A. Zenin and S. I. Bozhevolnyi, *ACS Photonics*, 2017, **4**, 943–949.
26 E. Arbabi, S. M. Kamali, A. Arbabi and A. Faraon, *ACS Photonics*, 2018, **5**, 3132–3140.
27 P. C. Wu, J. W. Chen, C. W. Yin, Y. C. Lai, T. L. Chung, C. Y. Liao, B. H. Chen, K. W. Lee, C. J. Chuang, C. M. Wang and D. P. Tsai, *ACS Photonics*, 2017, **5**, 2568–2573.
28 S. Wei, Z. Yang and M. Zhao, *Opt. Lett.*, 2017, **42**, 1580–1583.
29 F. Ding, Y. Chen and S. I. Bozhevolnyi, *Appl. Sci.*, 2018, **8**, 594.
30 Z. H. Jiang, L. Lin, D. Ma, S. Yun, D. H. Werner, Z. Liu and T. S. Mayer, *Sci. Rep.*, 2014, **4**, 7511.
31 S. Kruk, B. Hopkins, I. I. Kravchenko, A. Miroshnichenko, D. N. Neshev and Y. S. Kivshar, *APL Photonics*, 2016, **1**, 030801.
32 D. Wen, F. Yue, W. Liu, S. Chen and X. Chen, *Adv. Opt. Mater.*, 2018, **6**, 1800348.
33 Y. Yang, W. Wang, P. Moitra, I. I. Kravchenko, D. P. Briggs and J. Valentine, *Nano Lett.*, 2014, **14**, 1394–1399.
34 F. Ding, Z. Wang, S. He, V. M. Shalaev and A. V. Kildishev, *ACS Nano*, 2015, **9**, 4111–4119.
35 N. Zhou and J. Wang, *Sci. Rep.*, 2018, **8**, 8038.
36 G. Zheng, H. Mühlenbernd, M. Kenney, G. Li, T. Zentgraf and S. Zhang, *Nat. Nanotechnol.*, 2015, **10**, 308–312.
37 D. Wen, F. Yue, G. Li, G. Zheng, K. Chan, S. Chen, M. Chen, K. F. Li, P. W. H. Wong, K. W. Cheah, E. Y. B. Pun, S. Zhang and X. Chen, *Nat. Commun.*, 2015, **6**, 6241.
38 B. H. Chen, P. C. Wu, V. C. Su, Y. C. Lai, C. H. Chu, I. C. Lee, J. W. Chen, Y. H. Chen, Y. C. Lan, C. H. Kuan and D. P. Tsai, *Nano Lett.*, 2017, **17**, 6345–6352.
39 R. Zhao, L. Huang, C. Tang, J. Li, X. Li, Y. Wang and T. Zentgraf, *Adv. Opt. Mater.*, 2018, **6**, 1800490.
40 X. Zang, F. Dong, F. Yue, C. Zhang, L. Xu, Z. Song, M. Chen, P. Y. Chen, G. S. Buller, Y. Zhu, S. Zhuang, W. Chu, S. Zhang and X. Chen, *Adv. Mater.*, 2018, **30**, 1707499.
41 D. Lin, P. Fan, E. Hasman and M. L. Brongersma, *Science*, 2014, **345**, 298.
42 F. Qin, L. Ding, L. Zhang, F. Monticone, C. C. Chum, K. Deng, S. Mei, Y. Li, J. Teng, M. Hong, S. Zhang, A. Alù and C. W. Qiu, *Sci. Adv.*, 2016, **2**, e1501168.
43 P. C. Wu, W. Y. Tsai, W. T. Chen, Y. W. Huang, T. Y. Chen, J. W. Chen, C. Y. Liao, C. H. Chu, G. Sun and D. P. Tsai, *Nano Lett.*, 2017, **17**, 445–452.
44 Z. Liu, Z. Li, Z. Liu, H. Cheng, W. Liu, C. Tang, C. Gu, J. Li, H. T. Chen, S. Chen and J. Tian, *ACS Photonics*, 2017, **4**, 2061–2069.
45 J. P. B. Mueller, N. A. Rubin, R. C. Devlin, B. Groever and F. Capasso, *Phys. Rev. Lett.*, 2017, **118**, 113901.
46 L. Wu, J. Tao and G. Zheng, *Phys. Rev. B: Condens. Matter*, 2018, **97**, 245426.
47 B. Wang, F. Dong, H. Feng, D. Yang, Z. Song, L. Xu, W. Chu, Q. Gong and Y. Li, *ACS Photonics*, 2018, **5**, 1660–1664.
48 F. Zhang, M. Pu, J. Luo, H. Yu and X. Luo, *Opto-Electron. Eng.*, 2017, **44**, 319–325.
49 G. Yoon, D. Lee, K. T. Nam and J. Rho, *Sci. Rep.*, 2018, **8**, 9468.
50 C. S. Park, V. R. Shrestha, W. Yue, S. Gao, S. S. Lee, E. S. Kim and D. Y. Choi, *Sci. Rep.*, 2017, **7**, 2556.
51 G. Yoon, D. Lee, K. T. Nam and J. Rho, *ACS Nano*, 2018, **12**, 6421–6428.
52 N. Mahmood, I. Kim, M. Q. Mehmood, H. Jeong, A. Akbar, D. Lee, M. Saleem, M. Zubair, M. S. Anwar, F. A. Tahir and J. Rho, *Nanoscale*, 2018, **10**, 18323–18330.
53 Z. Zhou, J. Li, R. Su, B. Yao, H. Fang, K. Li, L. Zhou, J. Liu, D. Stellinga, C. P. Reardon, T. F. Krauss and X. Wang, *ACS Photonics*, 2017, **4**, 544–551.
54 D. Sell, J. Yang, S. Doshay, K. Zhang and J. A. Fan, *ACS Photonics*, 2016, **3**, 1919–1925.
55 H. Liang, Q. Lin, X. Xie, Q. Sun, Y. Wang, L. Zhou, L. Liu, X. Yu, J. Zhou, T. F. Krauss and J. Li, *Nano Lett.*, 2018, **18**, 4460–4466.
56 Z. Yin, F. Chen, L. Zhu, K. Guo, F. Shen, Q. Zhou and Z. Guo, *J. Mater. Chem. C*, 2018, **6**, 6354.
57 A. Zhan, S. Colburn, R. Trivedi, T. K. Fryett, C. M. Dodson and A. Majumdar, *ACS Photonics*, 2016, **3**, 209–214.
58 S. Gao, W. Yue, C. S. Park, S. S. Lee, E. S. Kim and D. Y. Choi, *ACS Photonics*, 2017, **4**, 322–328.

